Modelling kinetic energy dissipation of bouncing droplets for Lagrangian simulation of impinging sprays under high ambient pressures

Zhenyu Zhang[a], Peng Zhang[a,*]

[a] *Department of Mechanical Engineering, The Hong Kong Polytechnic University, Kowloon, Hong Kong*

Abstract: Binary droplet collision under high ambient pressures was investigated numerically by using the front tracking method. The particular interest of the investigation is to predict the kinetic energy dissipation of droplet bouncing, which tends to be the dominant collision outcome in the impinging sprays under high ambient pressures. A practically useful model was proposed based on the predicted kinetic energy dissipation and implemented in the KIVA-3V computer program code for the Lagrangian simulation of the free and impinging spray experiments under high ambient pressures. The results show that the model can make qualitatively satisfactory predictions to the spray shape, the tip penetration length, and the Sauter mean diameter (SMD).

Keywords: droplet collision; front tracking method; high pressure; kinetic energy dissipation; impinging sprays.

First author:
E-mail: zhenyu.zhang@polyu.edu.hk.
* Corresponding author
FG 608, The Hong Kong Polytechnic University Hung Hom, Kowloon, Hong Kong, China;
E-mail: pengzhang.zhang@polyu.edu.hk.
Fax: (852)23654703, Tel: (852)27666664.

NOMENCLATURE

Non-dimensional parameters and variables

We Weber number

B Impact parameter

DE Dissipation energy

f_E Kinetic energy dissipation factor

KE Kinetic energy

Oh Ohnesorge number

T Time

TVDR Total viscous dissipation rate

Φ Local viscous dissipation rate

Δ Size ratio

Dimensional parameters and variables

$\boldsymbol{V}$ Velocity vector

$\boldsymbol{n}$ Unit normal vector

$\boldsymbol{x}$ Space vector

ρ Density

μ Viscosity

p Pressure

U Relative velocity

R Radius

t Time

σ Surface tension

π pi

τ Natural oscillation time

S Distance

u Velocity component along the r-direction

w Velocity component along the z-direction

Δ Difference

a, b, c Constant

Subscripts

cr Critical

l Liquid

g Gas

L Larger droplet

S Smaller droplet

f Interface

0 Initial

B Bouncing

E Energy

t Tip and impingement point

z1 Nozzle 1 and impingement point

z2 Nozzle 2 and impingement point

n New droplets

i, j Serial number

Superscripts

$*$ Modified

$'$ After bouncing

Abbreviation

FTM Front tracking method

SMD Sauter mean diameter

1. Introduction

Dynamics of droplet collision under high ambient pressures is relevant to many spray phenomena in combustion energy conversion devices. A prominent example is the droplet collision in the dense spray region near the fuel injectors in the compression ignition internal combustion engines, gas turbine engines, and rocket engines. Frequent droplet collisions occur because of the high droplet number density and complex irregular airflow in the combustion chamber. The collision outcomes, such as droplet bouncing, coalescence and separation, can significantly influence the droplet size and number density; the post-collision droplet velocity can substantially change the droplet spatial distribution. It is well known that droplet size and spatial distributions are crucial factors determining the combustion and emission performance of engines (Law, 2010).

Earlier experimental investigation on droplet collision was motived by understanding the raindrop formation in the atmospheric environment (Abbott, 1977; Adam et al., 1968; Brazier-Smith et al., 1972; Gunn, 1965; Magarvey and Geldart, 1962). Two collision outcomes of binary water droplets, either coalescence or stretching separation, were found to depend on the collision Weber number, We, the impact parameter, B, and the size ratio, Δ. Here, We measures the relative importance of the droplet inertia compared with the surface tension; B represents the deviation of the trajectory of droplets from that of head-on collision, with $B = 0$ denoting the head-on collision and $B =1$ the grazing collision; Δ is usually defined as the radius ratio of the larger droplet to the smaller one. Additional parameters, such as Ohnesorge number, Oh, which compares the viscous force with inertial and surface tension forces, and the density and viscosity ratios of liquid and gas, may be required when the viscous dissipation and ambient pressure are taken into account (Zhang and Law, 2011).

By recognizing liquid alkanes is practically relevant to combustion engines, Jiang et al. (1992) and Qian and Law (1997) experimentally investigated the collision dynamics of equal-size alkane (n-heptane, n-dodecane and n-tetradecane) droplets. They observed frequent droplet bouncing, which

was hardly seen in the experiment on water droplets. The droplet bouncing phenomenon was later confirmed by Estrade et al. (1999) for equal size ethanol droplets and Tang et al. (2012) for unequal-size tetradecane droplets.

Qian and Law (1997) also extended their experiment from atmospheric environment to other gaseous environment (nitrogen, helium and ethylene) under reduced and elevated pressures from 0.6 atm to 12 atm. Their results show that increasing ambient pressure significantly promotes droplet bouncing. For this reason, although bouncing is rarely seen for water droplets at atmospheric pressure, it is can be readily observed at high ambient pressure. Similarly, droplet bouncing tends to be a dominant outcome for alkane droplets at high ambient pressure unless the collision Weber number is unusually large to cause droplet separation or splashing.

To understand the pressure effects, Zhang and Law (2011) theoretically analyzed the equal-size droplet collision and found that the gas pressure affects droplet collision by modifying the dynamics of the gas film between two colliding surface. Specifically, in the reduced pressure environment, the gas film has lower density and hence is readily drained out, implying tendency of coalescence. At elevated pressures, the denser gas film is harder to be drained out, leading to increased resistance force on the droplet by the substantial pressure buildup in the film and therefore the large droplet deformation. Droplet bouncing occurs if the film thickness is insufficiently small to trigger the van der Waals attraction force when all the collisional kinetic energy is either converted to other forms or dissipated by viscosity. Zhang et al. (2016b) numerically confirmed that droplet collision tend to bounce off with increasing the ambient pressure by using molecular dynamics. Li's (2016) simulation also confirmed colliding droplets tend to bounce off under high ambient pressures by implementing Zhang and Law's (2011) theoretical model for the rarefied dynamics of gas film. Dupuy et al. (2011) numerically simulated the head-on collision of two-dimensional droplets up to 150 atm by using Lattice Boltzmann method combined with a free energy approach.

Extensive advances have been achieved in modelling droplet collision in sprays and spray combustion. Majority of the previous work on droplet collision modelling was motived by improving the O'Rourke's (1981) model, which was simplistically developed based on the early experimental observations for water droplets (Brazier-Smith et al., 1972). These works mainly focus on estimating the droplet collision probability (Nordin, 2001; Perini and Reitz, 2016; Schmidt and Rutland, 2000; Taskiran and Ergeneman, 2014; Zhang et al., 2012) and reproducing the complex collision outcomes (Kim et al., 2009; Munnannur, 2007b; Munnannur and Reitz, 2007; Munnannur and Reitz, 2009; Tennison et al., 1998; Zhang et al., 2016b) from experiment and analysis (Ashgriz and Poo, 1990; Estrade et al., 1999; Jiang et al., 1992; Qian and Law, 1997). However, few studies attempted to determine the post-collision characteristics of droplets, especially under high ambient pressure.

It has been recognized that (Jiang et al., 1992; Qian and Law, 1997; Zhang and Zhang, 2017) droplet collision is inelastic and that the viscous dissipation in the deforming droplets can be substantial. To account for the energy dissipation after droplet bouncing, O'Rourke (1981) defined a kinetic energy dissipation factor, $f_E = 1 - KE'/KE$, where KE and KE' are the droplet total kinetic energy before and after bouncing, respectively. O'Rourke proposed an empirical model as

$$f_E = 1 - \left(\frac{B - B_{cr}}{1 - B_{cr}}\right)^2, B_{cr} = \sqrt{min\,(1.0, [2.4f(\Delta)/We])}, f(\Delta) = \Delta^3 - 2.4\Delta^2 + 2.7\Delta^1 \qquad (1)$$

where B_{cr} is the transition impact parameter from coalescence ($B \leq B_{cr}$) to grazing ($B > B_{cr}$). This model was implemented in the widely-used KIVA computer program (Amsden et al., 1989) and employed by many subsequent numerical simulations on spray combustion (Kim et al., 2009; Munnannur, 2007a; Munnannur and Reitz, 2007; Munnannur and Reitz, 2009). The experimental results of Jiang et al. (1992) and Qian and Law (1997) indicate that f_E can be as large as 0.5 at large Weber numbers. Zhang et al. (2016b; 2017) used $f_E = 0.5$ as an approximation in their numerical simulations of non-reacting impinging sprays under elevated ambient pressures and of impinging spray combustion in the opposed-piston compression ignition engine.

Whereas ambient pressure has been proved to have significant influence on the collision outcomes, it was surprising to find that the dependence of f_E on various collision parameters, such as *We*, Δ and *Oh*, has not been accurately quantified in the previous works until most recently the authors (Zhang and Zhang, 2017) conducted a numerical study by using front tracking method (referred to as FTM hereinafter). The simulation results were validated by Zhang and Law's (2011) theory and previous experiments for both equal-size (Pan and Yin, 2012) and unequal-size droplet collision (Tang et al., 2012) under atmospheric pressure. The results show that most viscous dissipation occurs in the early stage of collision, and that increasing the size ratio enhances the viscous dissipation. A practically useful model for estimating f_E was proposed and validated, but the effect of ambient pressure was not considered.

In the present study, we first extended our previous numerical study (Zhang and Zhang, 2017) on kinetic energy dissipation of droplet bouncing from atmospheric environment to high pressure environment, in order to develop a modified model for estimating pressure-dependent $f_E(p)$. Subsequently, we numerically simulated the impinging spray experiments in the literature by employing KIVA-3V computer program implemented with the model. We shall present the numerical methodology for droplet collision and non-reacting impinging spray simulations, in Section 2. Simulation results and experimental validation on droplet bouncing and on impinging sprays at elevated pressures shall be presented in Section 3 and Section 4, respectively.

2. Numerical methodology

The present numerical simulation contains two parts. First, droplet collision of different size ratios under various ambient pressures were calculated and analyzed to modify the previous kinetic energy dissipation factor, which was subsequently implemented into the KIVA-3V computer program to simulate the free and impinging spray characteristics of Chiba et al. (2000) and Maruyama et al. (2001). More details are as follows.

2.1 Binary droplet collision

Binary droplet collision was simulated by using the FTM for its high accuracy in simulating droplet bouncing for both equal-size (Pan and Yin, 2012) and unequal-size (Zhang and Zhang, 2017) situations. The present FTM was first developed by Tryggavason and his colleagues (Nobari et al., 1996; Tryggvason et al., 2001; Unverdi, 1990; Unverdi and Tryggvason, 1992) to track interface in a Lagrangian framework, while solve the multiphase flow in a unified domain and in a grid of Eulerian coordinates. To accurately simulate the present problem of droplet bouncing, which is a typical multiscale one, we need to resolve the intervening gas film, which is about $O(10^2 - 10^3)$ times smaller than the droplet diameter. Thus, the most desirable advantages of the FTM method are that it can accurately track the evolution of interfaces without the loss of mass conservation of different phases and that the computation cost is less demanding than those mesh-sensitive methods such as Volume of Fluid (Gotaas et al., 2007; Nikolopoulos et al., 2012) and Level Set method (Pan and Suga, 2005).

The adopted FTM has been detailedly introduced in the literature (Unverdi, 1990; Unverdi and Tryggvason, 1992) and implemented in an axisymmetric flow solver which was used by Nobari et al. (1996), Qian (1997), and Pan et al. (2008) for equal-size droplet collision. Recognizing that collision between two unequal-size droplets is more relevant to practical situation, one of the present authors (Liu et al., 2013) adopted the FTM to simulate the unequal-size droplet coalescence and inter-mixing processes. Subsequently, the authors (Zhang and Zhang, 2017) employed the FTM to study the viscous dissipation of unequal-size droplet collision.

For a brief summary of the FTM, a conservative, second-order centered difference scheme for the spatial variables and an explicit first-order time integration method were used to solve the unsteady Navier-Stokes equation for incompressible flows in both gas and liquid phases, given by

$$\frac{\partial(\rho \boldsymbol{V})}{\partial t} + \nabla \cdot (\rho \boldsymbol{V}\boldsymbol{V}) = -\nabla p + \nabla \cdot \mu[\nabla \boldsymbol{V} + (\nabla \boldsymbol{V})^T] - \sigma \int k\boldsymbol{n}\delta(\boldsymbol{x} - \boldsymbol{x}_f)dA \quad (2)$$

where $\boldsymbol{V}$, ρ, μ and, p are the velocity vector, density, viscosity and pressure, respectively. The subscripts "l" and "g" are used to denote the liquid and gas phases, and the subscripts "L" and "S" the larger and smaller droplets. Surface tension, whose coefficient is denoted by σ, is implanted as a delta function integrated locally over the immiscible interface so as to render a singular force exerted on the flow field. k is twice the mean curvature, $\boldsymbol{n}$ the unit vector outwardly directing from the droplet surface, and $\boldsymbol{x}$ the space vector with the subscript "f" designating the interface. The interface separating the two phases is tracked by using Lagrangian marker particles. Following the previous studies (Pan et al., 2008; Zhang and Zhang, 2017), we neglected the influence of gravity on the droplet collision for the following reasons. First, the droplet Bond number ($Bo = \Delta\rho g R_s^2/\sigma$) in the present problem is about 2.87×10^{-3}, indicating the insignificant effect of gravity on droplet deformation. Second, as will be shown shortly in Section 3.1, the whole process of droplet bouncing concerned in the present study lasts for around 1.0 ms, during which the gravity accelerates the droplets by about 0.01 m/s, which is two orders of magnitude smaller than the droplet relative velocity (i.e., 0.64 m/s for soft bouncing and 1.12m/s for hard bouncing).

The present numerical study considers only head-on droplet collision (i.e., B =0), which are intrinsically axisymmetric with respect to the axis connecting the two droplet mass centers. It should be noted that all the variables in the present simulation are non-dimensional, the governing equations are non-dimensionalized by using three independent quantities, such as the smaller droplet radius R_s, the relative velocity U, and the liquid density ρ_l. It should be noted that most droplet collisions are not perfect head-on collisions. The more realistic off-center collisions (0<B<1) have been experimentally (Ashgriz and Poo, 1990) and numerically (Chen et al., 2011; Gotaas et al., 2007) studied, and some useful discoveries have been made. However, the primary objective of this study is to investigate the influence of high ambient pressure on the colliding droplets, which was barely

studied in the literature. The pressure effect is very meaningful for engine relevant conditions and could be widely used in engine simulations. Consequently, to avoid the extreme complexity of dealing with the pressure effect and the off-center collision in the same time, the present simulation on binary droplet collision was focused on the ideal situation of head-on collision (B=0). The adopted numerical code based on the front tracking method has been sufficiently validated by a number of previous studies (Kuan et al., 2014; Nobari et al., 1996; Pan et al., 2008; Pan and Yin, 2012; Singh and Shyy, 2007; Zhang et al., 2016a) for atmospheric pressure, and further validated in the present study for high pressures.

The collision Weber number is defined as $We = 2\rho_l U^2 R_S/\sigma$, the Ohnesorge number $Oh = 16\mu_l(\rho_l R_S \sigma)^{-1/2}$, the liquid Reynolds number $Re_l = 2\rho_l U R_S/\mu_l = 16\sqrt{2We}/Oh$, and the size ratio $\Delta = R_L/R_S$. The effects of viscosity ratio, μ_g/μ_l on the droplet deformation and viscous dissipation can be neglected because of the two or three orders of magnitude smaller than unity, as has been confirmed in the previous studies (Pan and Yin, 2012; Unverdi, 1990; Unverdi and Tryggvason, 1992). The governing equations are non-dimensionalized by using the radius of the smaller droplet R_s (degenerate to R for equal-size droplets), the relative velocity U, and the liquid density ρ_l. Consequently, the non-dimensional time is $T = 2R_s/Ut$, where t is the real time. To facilitate the comparison with the previous experimental and numerical studies, a characteristic natural oscillation time of droplet (Lamb, 1932) is used and defined by $\tau = \pi(2\rho_l R_s^3/\sigma)^{1/2}/4$, which is related to T by $T = We^{-\frac{1}{2}}\tau/t$.

The detailed description of the present computational domain and the grid-independence study can be found in our previous study (Zhang and Zhang, 2017). For a brief description, a cylindrical coordinate (r, z) axisymmetric domain was used with $16R_L$ in length and $3R_L$ in radius, as shown in Figure 1(a). The computational domain is discretized by a uniform structured, orthogonal, staggered mesh consisting of 132 nodes in the r-direction and 704 nodes in the z-direction. The

axisymmetric boundary condition is specified to the axis and out-flow boundary conditions are specified to the other boundaries.

2.2 Numerical simulation of Impinging sprays

As an application of the present model for kinetic energy dissipation factor $f_E(p)$, we simulated Chiba et al.'s (2000) and Maruyama et al.'s (2001) experiments on the free and three types of impinging spray in a constant-volume chamber filled with nitrogen of 10 atm. It is noted that these experiments provide spray shape shadowgraphs and droplet size distributions for validation.

In the impinging spray experiment, two sprays from two separate single-nozzle injectors with 0.25 mm in diameter were impinged in a chamber. The injection pressure is 19.6 MPa and the duration is 2.0 ms. The simulation adopted a three-dimensional cubic computational domain of $120 \times 120 \times 120\ mm^3$ with 216,000 cells, as shown in Figure 1(b). The grid-independence can be seen in our previous publication (Zhang et al., 2016b) and similar cell size was also used by Kim et al. (2009) for simulating the same impinging sprays. Liquid fuel was injected into the chamber in the form of droplet parcels of the nozzle radius. The initial droplet number density is 100 parcels/mg. The computational time step was set as 2×10^{-3} ms. The domain boundary temperature was set as the 298 K and with the nonslip condition for velocity.

The standard k-ε model (Amsden et al., 1989), the TAB model (O'Rourke and Amsden, 1987) were employed to account for turbulent flow and droplet aerodynamic breakup, respectively. The SIMPLEC method was used for velocity-pressure coupling and the Spalding model (O'Rourke, 1981) was adopted for modelling evaporation. It is emphasized that more sophisticated while complex methods for modelling turbulent flow, droplet breakup and evaporation, and fuel chemistry, were fully recognized but not employed in the present study, in order to facilitate the clarification of the role of droplet collision in spray impingement.

To account for the frequent droplet collision, a recently proposed pressure-dependent droplet collision model (Zhang et al., 2016b) was adopted in this simulation to account for the experimental observation of Qian and Law (1997) and theoretical results of Zhang and Law (2011) that increasing ambient pressure promotes droplet bouncing, which however has not been considered in the previous droplet collision models. By using the pressure-dependent kinetic energy dissipation factor f_E to be elucidated in the following text, the free and impinging sprays was simulated and analyzed to reveal its important implications.

3. Droplet bouncing under high ambient pressure

3.1 Experimental validation

The FTM method has been sufficiently validated for droplet bouncing under atmospheric pressure in the previous works (Nobari et al., 1996; Pan et al., 2008; Zhang and Zhang, 2017). However, due to the relatively low spatial resolutions in the earlier experiments, it is impossible to examine the details about droplet deformation. The high quality shadowgraph images of droplet collision at atmospheric pressure can be found in Pan et al.'s (2008) experiment for equal-size droplets and Tang et al.'s (2012) experiment for equal- and unequal-size droplets. Both experiments have been used to validate the present computational methodology in the authors' recent work (Zhang and Zhang, 2017). Here, we only considered two representative bouncing cases from Tang et al.'s (2012) experiment, which have not been simulated in the previous works.

Following the notations used in the previous studies (Pan et al., 2008; Zhang and Zhang, 2017), we used the "soft" and "hard" bouncing to denote the bouncing after minor deformation and after substantial deformation, respectively. For both the "hard" bouncing case at *We* =6.83, Δ=1.65, and *Oh* = 0.739, as shown in Figure 2(a), and the "soft" bouncing case at *We* =2.95, Δ=2.33 and *Oh* = 0.806, as shown in Figure 2(b), very good agreement can be seen throughout the entire process of droplet deformation and droplet bouncing. Only slight discrepancy can be observed in Figure 2(a) for

the larger droplet in the later stage such as at T=0.69 and at T=0.98. Several reasons can contribute to the small discrepancy. First, the numerical errors together the second-order finite difference method in solving the governing equation may cause errors in velocity flied and interface tracking. Second, the high liquid-gas density ratio and the extremely thin gas film between two interacting droplets can also result in numerical errors. Third, in the experiment, the larger droplet need more time to reach its maximum formation duo to the larger oscillation time τ, which may cause larger experimental uncertainties in time (Tang et al., 2012; Zhang and Zhang, 2017). Finally, for the unequal-size ratio collision, the larger size ratio and higher increases the probability of droplet off-center in the direction perpendicular to the image plane, which results in the measurement error of B.

To validate the present simulation of droplet bouncing under high ambient pressures, we simulated the experiment of Qian (1997) on head-on droplet collision under two different ambient pressures. Figure 3(a) compares the experimental and simulated evolutions of droplet deformation for the head-on collision of equal-size water droplets at We =2.26 and Oh =0.195 and the ambient pressure is 14.6 atm. The simulated droplet contours were selected at the same dimensional time instants when experimental images are available. Due to its low Weber number, the collision can be considered as “soft” bouncing. It is seen that the simulation shows good agreement with the experimental shadowgraphs in terms of droplet deformation and time sequence. Figure 3(b) shows the case of n-tetradecane droplet head-on collision at We =7.42 (a.k.a., “hard” bouncing), Oh =0.548 and the ambient pressure is 10 atm. Again, good agreement between the experimental and simulation results can be observed.

It should be noted that the experimental shadowgraph given in (Qian, 1997) are the only two sets of images for droplet collision under high ambient pressure in the literature. Although the present numerical methods based on FTM has been proved to be able to accurately predict droplet bouncing under atmospheric and high ambient pressures, further validation is still merited when new experimental data is available.

3.2 Viscous dissipation in bouncing droplets under high ambient pressure

It has been recognized that kinetic energy loss results from the viscous dissipation during droplet deformation. To represent the relative kinetic energy dissipation was introduced a time-dependent factor as

$$f_E(T) = DE(T)/KE(0) \tag{3}$$

where the accumulative dissipation energy at time T is calculated by

$$DE(T) = \int_{T_0}^{T} TVDR(T)dT = \int_{T_0}^{T} \iiint_{droplet\ volume} \Phi(\boldsymbol{x}, T)dVdT \tag{4}$$

TVDR is the total viscous dissipation rate within the droplets, Φ is the non-dimensional local viscous dissipation rate (White and Corfield, 2006)

$$\Phi = \mu\left[2\left(\frac{\partial u}{\partial r}\right)^2 + 2\left(\frac{u}{r}\right)^2 + 2\left(\frac{\partial w}{\partial z}\right)^2\right] + \mu(\frac{\partial u}{\partial z} + \frac{\partial w}{\partial r})^2 - \frac{2}{3}\mu\left[\frac{1}{r}\frac{\partial (ru)}{\partial r} + \frac{\partial w}{\partial z}\right]^2 \tag{5}$$

and $KE(0)$ is the initial kinetic energy before collision. It should be noted that, the last item in Eq. (5) vanishes for incompressible flows. We are particularly interested in the kinetic energy dissipation factor at the time, T_B, when the droplets are about to bouncing off, namely $f_E(T_B) = DE(T_B)/KE(0)$ (referred to as f_E hereinafter). This factor is crucial for the following droplet collision model for spray simulation.

Figure 4 shows the predicted TVDR (on the top graphs) and $f_E(T)$ (on the bottom graphs) of the n-tetradecane droplet bouncing for various Δs, *We* =7.3 and Oh=0.775 under four different ambient pressures (i.e., 1 atm, 10 atm, 50 atm and 100 atm) from collision starting time, $T = 0$, to the corresponding bouncing time, T_B. The time when the smaller droplet reaches its maximum deformation is also indicated in the graphs for each case.

Figure 4(a) and (b) show the TVDR and $f_E(T)$ for bouncing of equal-size droplets ($\Delta = 1$) under different ambient pressures. There is no significant difference among various cases in bouncing time which is about $T_B \approx 1.2$. Increasing ambient pressure reduces TVDR therefore results in the decreased $f_E(T)$. In addition, the maximum deformation times for the smaller droplet increases with the ambient pressure. Similar results can be seen in the bouncing of unequal-size droplets for Δ=1.46, 1.87 and 2.33, respectively, as shown in Figure 4(c)-(h).

To explain above observations, we showed in Figure 5 the vertical velocity component, v, (on the top half) and the pressure difference, ΔP, between the liquid and gas phase (on the bottom) at the maximum TVDR time instant for different Δs and ambient pressures. It should be noted that v, ΔP and TVDR are all non-dimensional quantities, which respectively denote v/U, $\Delta p/\rho_l U^2$, and $\Phi/(\rho_l U^3/R_s)$. Significant ΔP can be observed around the interface of colliding droplets, where substantial deformation occurs. Increasing the ambient pressure results in reduced ΔP while exerts greater resistance force on the deceleration of the centers of mass of the droplets. Consequently, the colliding surface of a droplet is quickly decelerated to a significantly small (but nonzero) velocity while the center of mass of the droplet remains its inertia. The velocity difference drives the droplet mass to move outwardly, against the surface tension, to deform the droplet. The vertical velocity component inside the droplets, v, can be treated as an indicator of droplet deformation speed. It is seen that, v, also decreases with increasing the ambient pressure, implying that the maximum deformation time instant for the smaller droplet increases due to the slower droplet deformation.

To further quantitatively explain why increasing ambient pressure reduces the viscous dissipation of colliding droplets, we compared the maximum deformation extent for various Δs under different ambient pressures, as shown in Figure 6. It is seen that droplet deformation is more significant at lower ambient pressures. This again can be understood by that the higher ambient pressure acts the greater resistance force on the deceleration of the centers of mass of the droplets result in the less deformation extent on the colliding droplets. The smaller droplet deformation extent

together with the longer time to achieve maximum deformation under higher ambient pressure imply smaller strain rates and hence smaller viscous dissipation.

Figure 7 compares the VDR distribution in the collision droplets at maximum VDR time instant. It has been recognized that the maximum VDR appears in the vicinity around the colliding interfaces (Zhang and Zhang, 2017). For the case of Δ=1.0, the VDR distribution is not uniform at atmospheric pressure, which increases from the interface center to the interface rim, where significant velocity difference, pressure difference and streamline deflection can be found, indicating the flow near the rim has larger local strain rates. As the ambient pressure increases to 10 atm, the VDR difference between interface center and rim diminishes then finally disappears at 50 and 100 atm. The concentrated VDR distribution can be treated as a boundary-layer-like flow problem, which has been theoretically analyzed by Zhang and Law (2011) and numerically verified in Zhang and Zhang's (2017) study. For the cases of unequal-size collision, the boundary-layer-like flow phenomenon also can be observed but tend to be insignificant under higher ambient pressures, due to the enlarged area of viscous dissipation and reduced VDR.

3.3 Kinetic energy dissipation factor

In the previous study, we have conducted a comprehensive parametric study to quantify the influence of *We*, Δ, and *Oh* on the energy dissipation factor f_E for head-on collision under atmospheric pressure. The results were reported as a model given by (Zhang and Zhang, 2017)

$$f_E = (We^* - We_{cr}^*)(c_1 Oh + c_2) + f_{E,cr} \tag{6}$$

where $We^* = We\Delta^3/[12(1+\Delta^3)(1+\Delta^2)]$ is the modified Weber number, representing the ratio of the total kinetic energy of the two droplets to their total surface energy (Rabe et al., 2010), We_{cr}^* the transition Weber number between coalescence and bouncing for head-on collision. $f_{E,cr} = 0.14\Delta + 0.275Oh + 0.134$ account for the fact that the viscous dissipation is nonzero for coalescence at smaller Weber numbers. For n-tetradecane droplet collision, $c_1 = -1.82, c_2 = 4.017$.

In the present study, we reexamined the above model to account for its pressure dependence based on the simulation results in Section. 3.2. Figure 8 shows the calculated kinetic energy dissipation factor $f_E(p)$ under different ambient pressures up to 100 atm. It should be noted that 2.3<*We*<12.3 is the experimentally determined Weber number range for bouncing of n-tetradecane droplets (B =0) under atmospheric pressure, according to Jiang et al.'s (1992) and Qian and Law's (1997) experimental observations.

By recognizing that $f_E(p)$ decreases with increasing the ambient pressure, p, a fitting formula was proposed as

$$f_E(p) = f_E(1)/[a(p-1)^2 + b(p-1) + 1] \tag{7}$$

where $f_E(1)$ is the kinetic energy dissipation factor under atmospheric pressure given in Equ. (6). It is seen that, all the simulation data are satisfactorily fitted by Eq. (7) with $a = 1.6 \times 10^{-5}$, $b = 5 \times 10^{-3}$ and $R^2 = 0.832$ for We=2.3; $R^2 = 0.838$ for We=7.3; $R^2 = 0.873$ for We =12.3.

To extend the head-on collision (B=0) to off-center collision (0< B <1), the proposed $f_E(p)$ was modified by using Chen et al.'s (2011) numerical results, given by

$$f_E(p) = (1 - B^2) \cdot \{f_E(1)/[a(p-1)^2 + b(p-1) + 1]\} \tag{8}$$

It is noted that Chen et al.'s (2011) modification $(1 - B^2)$ may not be sufficiently accurate for accounting for the impact parameter effect on the kinetic energy dissipation. However, the numerical investigation of off-center collisions is a very difficult task (Kuan et al., 2014; Singh and Shyy, 2007) for the front-tracking method because of the intrinsic 3D nature of the problem. The difficulty might be increased by the fact that the colliding droplets with varying B can result in droplet coalescence or separation, which pose a big challenge to the front-tracking method and are often studied by other numerical methods, for example the volume of fluid (VOF) and the level-set methods. A detailed

investigation on the influence of impact parameter B on the droplet collision certainly merits future studies.

Based on the above considerations, we proposed Equation 8 by fitting the present simulation results to obtain a practical approximation for predicting the viscous dissipation of head-on droplet collision (i.e. B=0) under high ambient pressures. We assumed that the effects of off-center collision (i.e. $B \neq 0$) and the ambient pressure are decoupled from each other, and therefore adopted the correction factor proposed by Chen et al. based on their 3D VOF numerical simulation. We fully recognized that both the "decoupling" assumption and the accuracy of Chen et al.'s (2011) correction must be further validated by more simulation studies in the future.

The post-collision velocities for droplet bouncing can be derived by accounting for the conservation of both energy and momentum during droplet collision process, given by (O'Rourke, 1981)

$$\boldsymbol{v}_{n,i} = \frac{\boldsymbol{v}_i R_i^3 + \boldsymbol{v}_j R_j^3 + R_j^3(\boldsymbol{v}_i - \boldsymbol{v}_j)\sqrt{1 - f_E(p)}}{R_i^3 + R_j^3} \quad (i, j = 1,2) \tag{9}$$

where $\boldsymbol{v}$ is the droplet velocities and R is the droplet radius. The subscript n denotes the new droplets after bouncing.

4. Lagrangian simulation of free and impinging sprays

To utilize the proposed pressure-dependent kinetic energy dissipation factor $f_E(p)$ for Lagrangian spray simulation, we considered Chiba et al.'s (2000) and Maruyama et al.'s (2001) experiment on the free and impinging sprays in a constant-volume chamber filled with nitrogen of 10 atm which provide a number of shadowgraph images and droplet size distributions, some of which have not been numerically reproduced in the previous studies.

As shown in Figure 9, Chiba et al. (2000) parameterized the impinging spray by using S_{Z1} as the distance between the left nozzle tip and the impingement point, S_{Z2} as the distance between the right nozzle tip and the impingement point, and S_t is the distance between impinging point and the spray tip. Thus, the spray tip penetration was defined as $S_{Z1} + S_t$. Specially, SMD of droplets at 2.0 mm above the spray tip at t = 2.0 ms was measured in the experiment. In the present study, we considered free spray and the impinging sprays with (Case A) $S_{Z1} = S_{Z2} = 14\,mm$, (Case B) $S_{Z1} = 15mm$ and $S_{Z2} = 45\,mm$ and (Case C) $S_{Z1} = S_{Z2} = 33\,mm$.

4.1 Experimental validation of spray shape

Figure 10 shows the experimental and numerical shadowgraph images and droplet spatial distributions at three different times for Case A. In particular, the experimental shadowgraph images (front view) at t =0.26 ms, 1.06 ms and 2.06 ms are shown in Figure 10(a), and the shadowgraph images (side view) are shown in Figure 10(c). Numerically predicted droplet size distribution and shadowgraph are illustrated in Figure (b) and (d).

It is seen that, there is no significant difference can be observed between the experimental and numerical results at t =0.26 ms, when the spray impingement has occurred just for a short while. The experiment was however not conducted without flaws: the slight non-synchronization between two impinging sprays can be seen from the front view of experimental shadowgraph images. This imperfection may be due to the pressure non-uniformity in the fuel supply system or the signal synchronization error in the control system, and it should not influence the comparison. After spray impingement, two sprays merge with each other, and a new swollen spray is generated. The atomization of spray is enhanced downstream of the impingement point as such the spray becomes wider. Regardless of slight discrepancy in droplet distribution near the impingement point, numerical prediction shows good agreement with experimental shadowgraph at t =1.06 ms. As the spray develops to t =2.06 ms when the fuel injection is just ended, the discrepancy between the experiment

and simulation is large—the experimental shadowgraph shows evidently asymmetry while the simulation results are symmetric from both views.

To investigate the impinging spray with asymmetric impingement, Figure 11 compares the experimental shadowgraphs and numerical results of Case B. It is noted that only the experimental shadowgraph images from the front view are available in Maruyama et al.'s (2001) experiment. Very good agreement between experimental and simulation results again can be observed at t =0.55 ms, when the spray impingement just occurs. No significant discrepancies are observed before the spray impingement because the sprays behave like two independent ones. Before $t = 0.55ms$, droplet collision frequency is relatively small and droplets are mainly affected by aerodynamic resistance and breakup. After spray impingement occurs and develops to t =1.15 ms, the numerical predictions also agree well with experimental shadowgraph images. Slight discrepancy can be seen around the tip of the lower spray as the numerical prediction produces a slightly longer penetration length. This may be attributed to the imperfect models for droplet collision and droplet breakup. In addition, we neglected the droplet evaporation in the present spray simulation, which certainly exists in the experiment and may have a significant influence on the macroscopic structures of the spray. The discrepancy become more significant at t =1.55 ms, when the fuel droplets near the tip of the lower spray are totally evaporated in the experimental shadowgraph.

4.2 Experimental validation of spray tip penetration

To further quantify the above comparison between the experimental and simulation results, Figure 12 shows the time-evolving spray tip penetration of three impinging sprays. For comparison, the results for free spray are also presented. For free spray tip penetration shown in Figure 12(a), droplet collision frequency is relatively low and spray characteristic is mainly affected by the aerodynamic deceleration and breakup of droplets. It is seen that the numerical prediction agree well

with the experimental result, indicating the present numerical framework is able to accurately predict droplet aerodynamic resistance and breakup.

For Case A shown in Figure 12(b), the simulation results again show good agreement with the experimental results. It is interesting to see that a "bend over" of spray penetration occurs after the spray impingement because the frequent droplet collisions result in increasing kinetic energy dissipation. Similar results also can be observed in Case B as shown in Figure 12 (c).

Figure 12(d) shows Case C for symmetric impingement with larger impingement distance. Compared with to Case A, the impinging spray in Case C has shorter spray tip penetration. This can be understood by that sprays with shorter impingement distance undergo less aerodynamic resistance before impingement and therefore results in larger droplet inertia that imply larger collision *We*. As discussed in the literature (Zhang and Zhang, 2017) and Section 3.3 that increasing the collision *We* enhances viscous dissipation and consequently causes smaller post-collision velocity of bouncing droplets.

To supplement the above quantitative comparison, Figure 13 shows the comparison between experimental and predicted SMD at the measurement point at t =2.0 ms. The experimental uncertainties of $\pm 10\%$ are also shown in the figure. It should be noted that the experimental data for Case B is unavailable in the literatures (Chiba et al., 2000; Maruyama and Saito, 2001). Several observations can be made from the comparison between the experimental results and numerical predictions as follow. First, all numerical predictions are within the experimental uncertainties. Second, Case A ($S_{Z1} = S_{Z2} = 14mm$) possess larger droplet size than Case C ($S_{Z1} = S_{Z2} = 33mm$) because the smaller impingement distance leads to more droplets with large collision, which tend to merge to increase their sizes. Third, all the numerical predictions slightly overshoot the measured data, probably because the present droplet collision model does not account for the occasional droplet separation, which tend to suppress droplet size growth.

5. Concluding remarks

Motivated by proposing physically meaningful and practically useful droplet collision model for simulating impinging sprays at high ambient pressures, the present simulation study was focused on modelling the kinetic energy dissipation of bouncing droplets and on applying the model to the Lagrangian simulation of sprays.

The first focus was to numerically investigate the influence of ambient pressure on the droplet viscous dissipation by using the front tracking method to simulate binary droplet collision. The sufficiently validated simulation shows that increasing the ambient pressure reduces the viscous dissipation rate. The physical reason is that the higher ambient pressure acts greater resistance force on decelerating the centers of mass of the droplets, results in the decrease of the droplet deformation speed and extent, consequently suppresses the viscous dissipation. Based on these numerical findings, A practically useful model for kinetic energy dissipation factor $f_E(p)$ which accounts for the ambient pressure effect was proposed as $f_E(p) = (1 - B^2)\{f_E(1)/[a(p-1)^2 + b(p-1) + 1]\}$ with $a = 1.6 \times 10^{-5}$, $b = 5 \times 10^{-3}$. This update model can degenerate to its previous version $f_E(1)$ for atmospheric pressure ($p = 1$).

To validate the model, we implemented it in the widely used computer program code KIVA-3V and simulated Chiba et al.'s (2000) and Maruyama et al.'s (2001) experiments on free and impinging sprays in the nitrogen of 10 atm. The qualitatively satisfactory agreement between the numerical and experimental results suggests that the present model can be treated as a practical approximation for predicting kinetic energy dissipation after droplet bouncing. Future experiments on droplet collision and sprays under high ambient pressures are desired to further validate the model.

Acknowledgements

The work was supported by the Hong Kong Research Grants Council/General Research Fund (PolyU 152217/14E and PolyU 152651/16E) and partly by “Open Fund” of State Key Laboratory of Engines (Tianjin University, No. K2018-12).

Reference

Abbott, C., A survey of waterdrop interaction experiments, *Rev. Geophys.*, vol. **15**, pp. 363-374, 1977.

Adam, J., Lindblad, N. and Hendricks, C., The collision, coalescence, and disruption of water droplets, *J. Appl. Phys.*, vol. **39**, pp. 5173-5180, 1968.

Amsden, A., O'Rourke, P. and Butler, T., Kiva-II: A computer program for chemically reactive flows with sprays, Los Alamos National Laboratory Rep. LA-11560-MS, 1989.

Ashgriz, N. and Poo, J., Coalescence and separation in binary collisions of liquid drops, *J. Fluid Mech.*, vol. **221**, pp. 183-204, 1990.

Brazier-Smith, P., Jennings, S. and Latham, J., The interaction of falling water drops: coalescence, *Proceedings of the Royal Society of London A: Mathematical, Physical and Engineering Sciences*. The Royal Society, 1972.

Chen, X., Ma, D., Khare, P. and Yang, V., Energy and mass transfer during binary droplet collision, Proceedings of 49th AIAA Aerospace Sciences Meeting Including the New Horizons Forum and Aerospace Exposition. 2011.

Chiba, T., Saito, M., Amagai, K. and Arai, M., Inter-spray impingement of two diesel sprays, *Proc. Int. Conf. Liquid Atomization and Spray Systems (ICLASS)*. 2000.

Dupuy, P. M., Lin, Y., Fernandino, M., Jakobsen, H. A. and Svendsen, H. F., Modelling of high pressure binary droplet collisions, *Computers Mathematics Applications*, vol. **61**, pp. 3564-3576, 2011.

Estrade, J.-P., Carentz, H., Lavergne, G. and Biscos, Y., Experimental investigation of dynamic binary collision of ethanol droplets–a model for droplet coalescence and bouncing, *Int. J. Heat Fluid Flow*, vol. **20**, pp. 486-491, 1999.

Gotaas, C., Havelka, P., Jakobsen, H. A., Svendsen, H. F., Hase, M., Roth, N. and Weigand, B., Effect of viscosity on droplet-droplet collision outcome: Experimental study and numerical comparison, *Phys. Fluids*, vol. **19**, pp. 102106, 2007.

Gunn, R., Collision characteristics of freely falling water drops, *Science*, vol. **150**, pp. 695-701, 1965.

Jiang, Y., Umemura, A. and Law, C., An experimental investigation on the collision behaviour of hydrocarbon droplets, *J. Fluid Mech.*, vol. **234**, pp. 171-190, 1992.

Kim, S., Lee, D. J. and Lee, C. S., Modeling of binary droplet collisions for application to inter-impingement sprays, *Int. J. Multiphas Flow*, vol. **35**, pp. 533-549, 2009.

Kuan, C. K., Pan, K. L. and Shyy, W., Study on high-Weber-number droplet collision by a parallel, adaptive interface-tracking method, *J. Fluid Mech.*, vol. **759**, pp. 30, 2014.

Lamb, H., *Hydrodynamics*, Cambridge university press, 1932.

Law, C. K., *Combustion physics*, Cambridge university press, 2010.

Li, J., Macroscopic Model for Head-On Binary Droplet Collisions in a Gaseous Medium, *Phys. Rev. Lett.*, vol. **117**, pp. 214502, 2016.

Liu, D., Zhang, P., Law, C. K. and Guo, Y., Collision dynamics and mixing of unequal-size droplets, *Int. J. Heat Mass Transfer*, vol. **57**, pp. 421-428, 2013.

Magarvey, R. and Geldart, J., Drop collisions under conditions of free fall, *J. Atmos. Sci.*, vol. **19**, pp. 107-113, 1962.

Maruyama, Y. and Saito, M., Effect of Inter-Impingement Process on the Behavior of a Diesel Spray, *In: Proc. ILASS-Asia*, vol. **2001**, pp. 241-246, 2001.

Munnannur, A., Droplet Collision Modeling in Multi-dimensional Engine Spray ComputationUniversity of Wisconsin Madison, 2007a.

Munnannur, A., Droplet Collision Modeling in Multi-dimensional Engine Spray Computation, ProQuest, 2007b.

Munnannur, A. and Reitz, R. D., A new predictive model for fragmenting and non-fragmenting binary droplet collisions, *International Journal of Multiphase Flow*, vol. **33**, pp. 873-896, 2007.

Munnannur, A. and Reitz, R. D., Comprehensive collision model for multidimensional engine spray computations, *Atomization Spray*, vol. **19**, pp., 2009.

Nikolopoulos, N., Strotos, G., Nikas, K. and Bergeles, G., The effect of Weber number on the central binary collision outcome between unequal-sized droplets, *Int. J. Heat Mass Transfer*, vol. **55**, pp. 2137-2150, 2012.

Nobari, M., Jan, Y. J. and Tryggvason, G., Head-on collision of drops-A numerical investigation, *Phys. Fluids*, vol. **8**, pp. 29-42, 1996.

Nordin, P., *Complex chemistry modeling of diesel spray combustion*, Chalmers University of Technology, 2001.

O'Rourke, P. J., *Collective drop effects on vaporizing liquid sprays,* Princeton University. New Jersey, 1981.

O'Rourke, P. J. and Amsden, A. A., The TAB method for numerical calculation of spray droplet breakup, 1987.

Pan, K.-L., Law, C. K. and Zhou, B., Experimental and mechanistic description of merging and bouncing in head-on binary droplet collision, *J. Appl. Phys.*, vol. **103**, pp. 064901, 2008.

Pan, K.-L. and Yin, G.-C., Parallel strategies of front-tracking method for simulation of multiphase flows, *Computers Fluids*, vol. **67**, pp. 123-129, 2012.

Pan, Y. and Suga, K., Numerical simulation of binary liquid droplet collision, *Phys. Fluids*, vol. **17**, pp. 082105, 2005.

Perini, F. and Reitz, R. D., Improved atomization, collision and sub-grid scale momentum coupling models for transient vaporizing engine sprays, *Int. J. Multiphas Flow*, vol. **79**, pp. 107-123, 2016.

Qian, J., Droplet and flame dynamics in combustion phenomena, Ph.D Thesis. Princeton University, 1997.

Qian, J. and Law, C., Regimes of coalescence and separation in droplet collision, *J. Fluid Mech.*, vol. **331**, pp. 59-80, 1997.

Rabe, C., Malet, J. and Feuillebois, F., Experimental investigation of water droplet binary collisions and description of outcomes with a symmetric Weber number, *Phys. Fluids*, vol. **22**, pp. 047101, 2010.

Schmidt, D. P. and Rutland, C., A new droplet collision algorithm, *J. Comput. Phys.*, vol. **164**, pp. 62-80, 2000.

Singh, R. and Shyy, W., Three-dimensional adaptive Cartesian grid method with conservative interface restructuring and reconstruction, *J. Comput. Phys.*, vol. **224**, pp. 150-167, 2007.

Tang, C., Zhang, P. and Law, C. K., Bouncing, coalescence, and separation in head-on collision of unequal-size droplets, *Phys. Fluids*, vol. **24**, pp. 022101, 2012.

Taskiran, O. O. and Ergeneman, M., Trajectory based droplet collision model for spray modeling, *Fuel*, vol. **115**, pp. 896-900, 2014.

Tennison, P. J., Georjon, T. L., Farrell, P. V. and Reitz, R. D., An Experimental and Numerical Study of Sprays from a Common Rail Injection System for Use in an HSDI Diesel Engine: SAE Paper 980810, 1998.

Tryggvason, G., Bunner, B., Esmaeeli, A., Juric, D., Al-Rawahi, N., Tauber, W., Han, J., Nas, S. and Jan, Y. J., A Front-Tracking Method for the Computations of Multiphase Flow, *J. Comput. Phys.*, vol. **169**, pp. 708-759, 2001.

Unverdi, S. O., *Numerical simulations of multi-fluid flows* Ph.D. Thesis. The University of Michigan, 1990.

Unverdi, S. O. and Tryggvason, G., A front-tracking method for viscous, incompressible, multi-fluid flows., *J. Comput. Phys.*, vol. **100**, pp. 25-37, 1992.

White, F. M. and Corfield, I., *Viscous fluid flow*, *3*, McGraw-Hill New York, 2006.

Zhang, J., Mi, J. and Wang, H., A new mesh-independent model for droplet/particle collision, *Aerosol. Sci. Tech.*, vol. **46**, pp. 622-630, 2012.

Zhang, P. and Law, C. K., An analysis of head-on droplet collision with large deformation in gaseous medium, *Phys. Fluids*, vol. **23**, pp. 042102, 2011.

Zhang, Y. R., Jiang, X. Z. and Luo, K. H., Bounce regime of droplet collisions: A molecular dynamics study, *J. Comput. Sci.*, vol. **17**, pp. 457-462, 2016a.

Zhang, Z., Chi, Y., Shang, L., Zhang, P. and Zhao, Z., On the role of droplet bouncing in modeling impinging sprays under elevated pressures, *Int. J. Heat Mass Transfer*, vol. **102**, pp. 657-668, 2016b.

Zhang, Z. and Zhang, P., Kinetic energy recovery and interface hysteresis of bouncing droplets after inelastic head-on collision, *Phys. Fluids*, vol. **29**, pp. 103306, 2017.

Zhang, Z., Zhang, P. and Zhao, Z., Spray Impingement and Combustion in a Model Opposed-Piston Compression Ignition Engine, *Combust. Sci. Technol.*, vol. **189**, pp. 1943-1965, 2017.

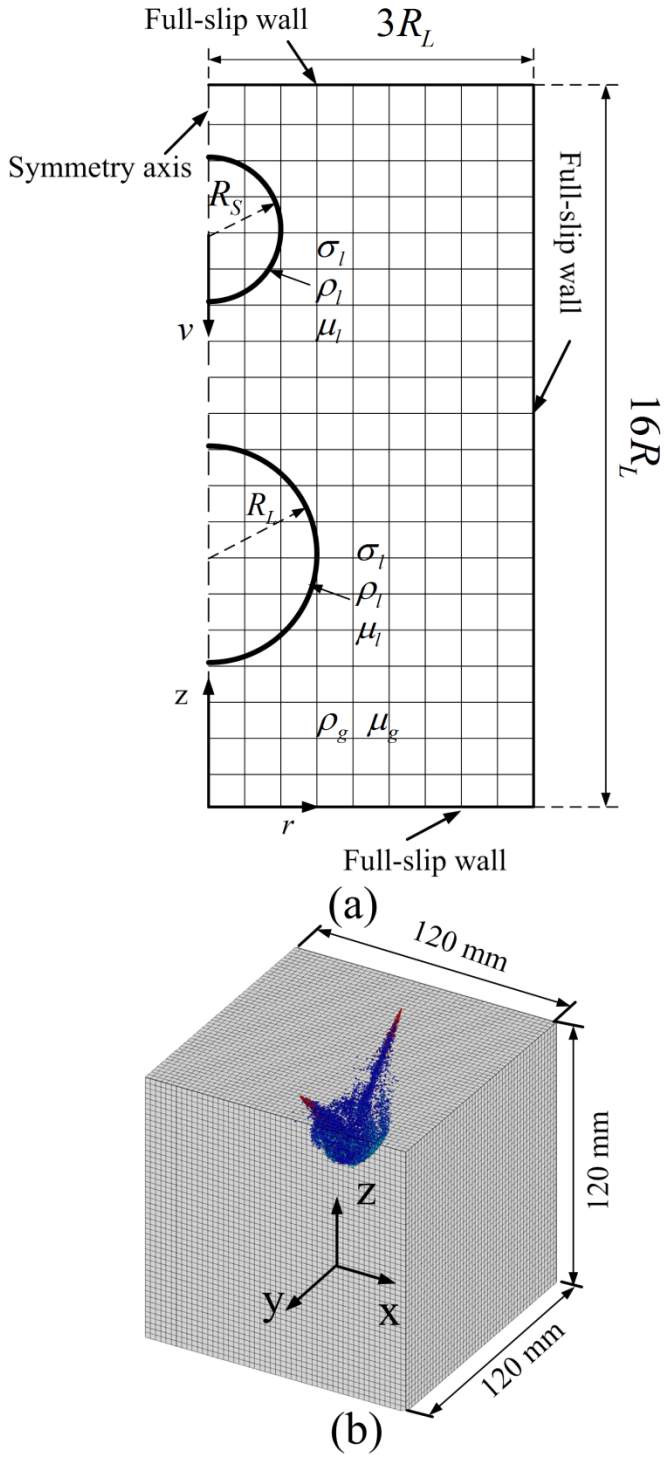

Figure 1. (a) axisymmetric computational domain, uniform structured grids, and boundary conditions for droplet bouncing calculation. (b) three-dimensional cubic computational domain for impinging spray calculation.

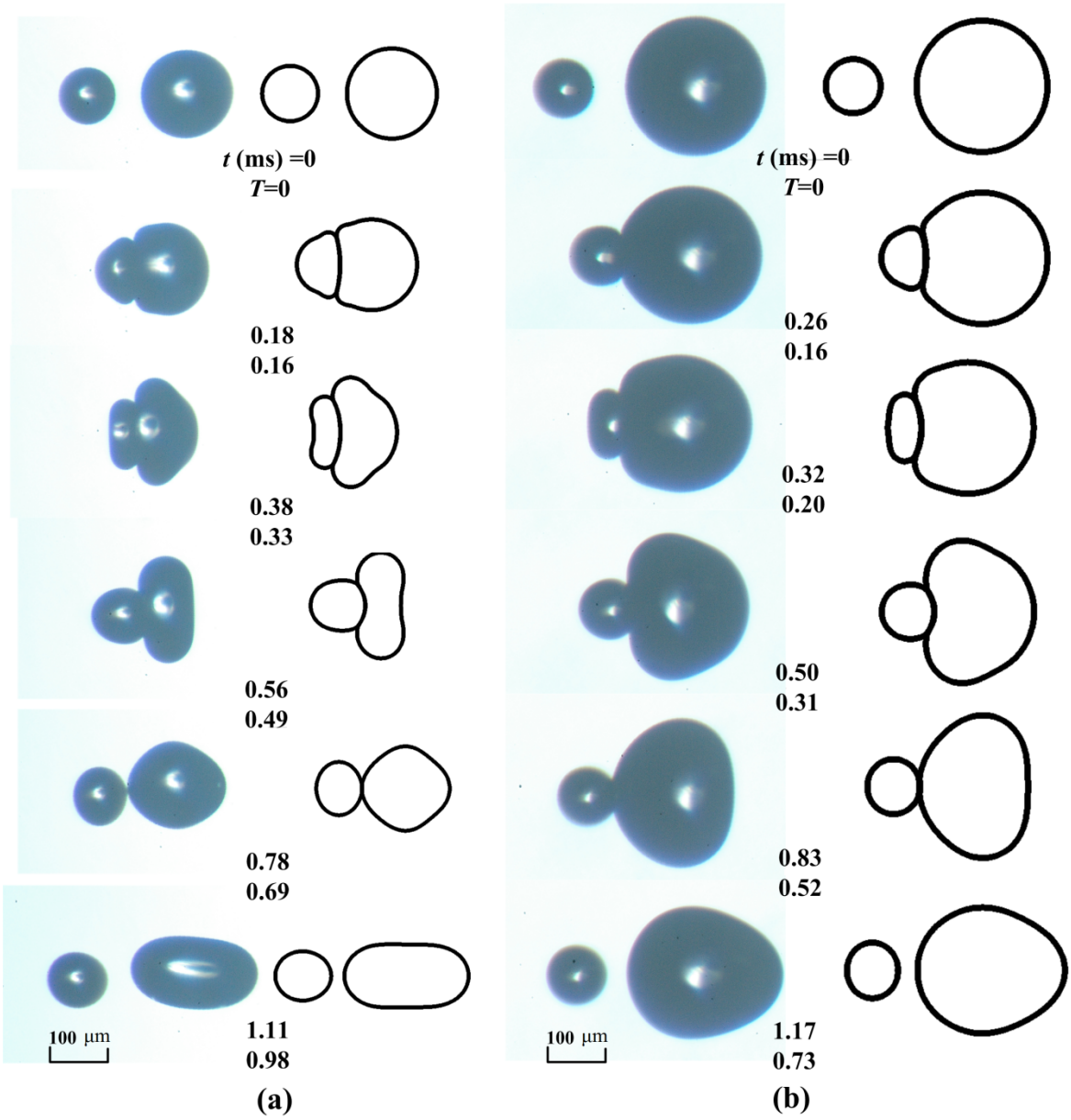

Figure 2. Time sequences of unequal-size droplet bouncing from the experimental images (shadow graphs) and the simulation results (thick solid lines) for n-tetradecane at atmospheric pressure. (a) We =6.83, Δ=1.65, Oh = 0.739 and R_s =109.6 μm, (b) We =2.95, Δ=2.33, Oh = 0.806 and R_s =92.5 μm.

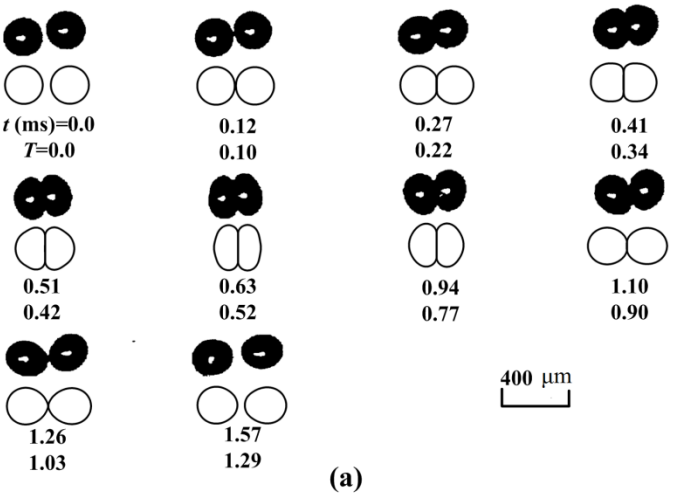

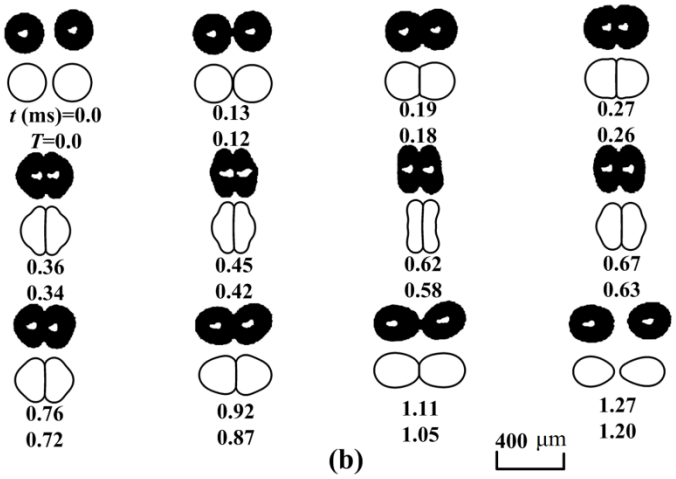

2

Figure 3. Time-sequence of droplet bouncing from the experimental images in Qian (1997) and from the computation (solid lines) for (a) water droplet collision in 14.6 atm argon with *We* = 2.26, *R* =200 μm, *Oh* = 0.195 and (b) n-tetradecane droplet collision in 10 atm nitrogen with *We* = 7.42, *R* =200 μm, *Oh* = 0.548.

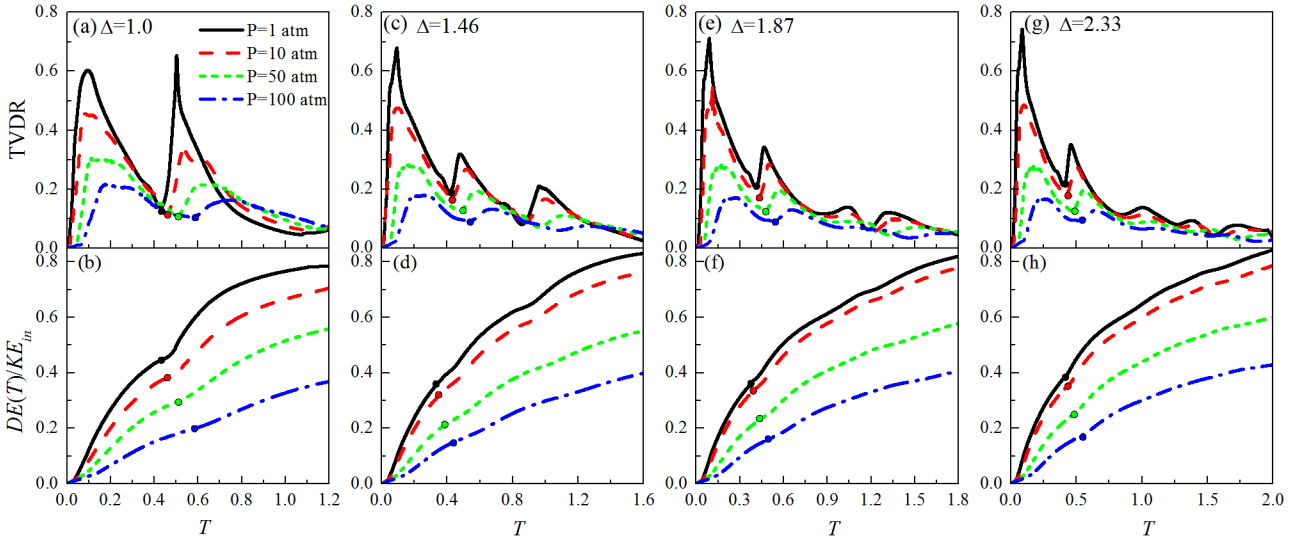

Figure 4. Evolution of TVDR (on the top graphs) and $DE(T)/KE(0)$ (on the bottom graphs) of the n-tetradecane droplet collision under various ambient pressures at *We*=7.3, *Oh*= 0.775 and R_s =100 μm. (a) and (b) Δ=1.0, (c) and (d) Δ=1.46, (e) and (f) Δ=1.87 and (g) and (h) Δ=2.33. Droplet maximum deformation time instants for smaller droplet are also indicated by circles.

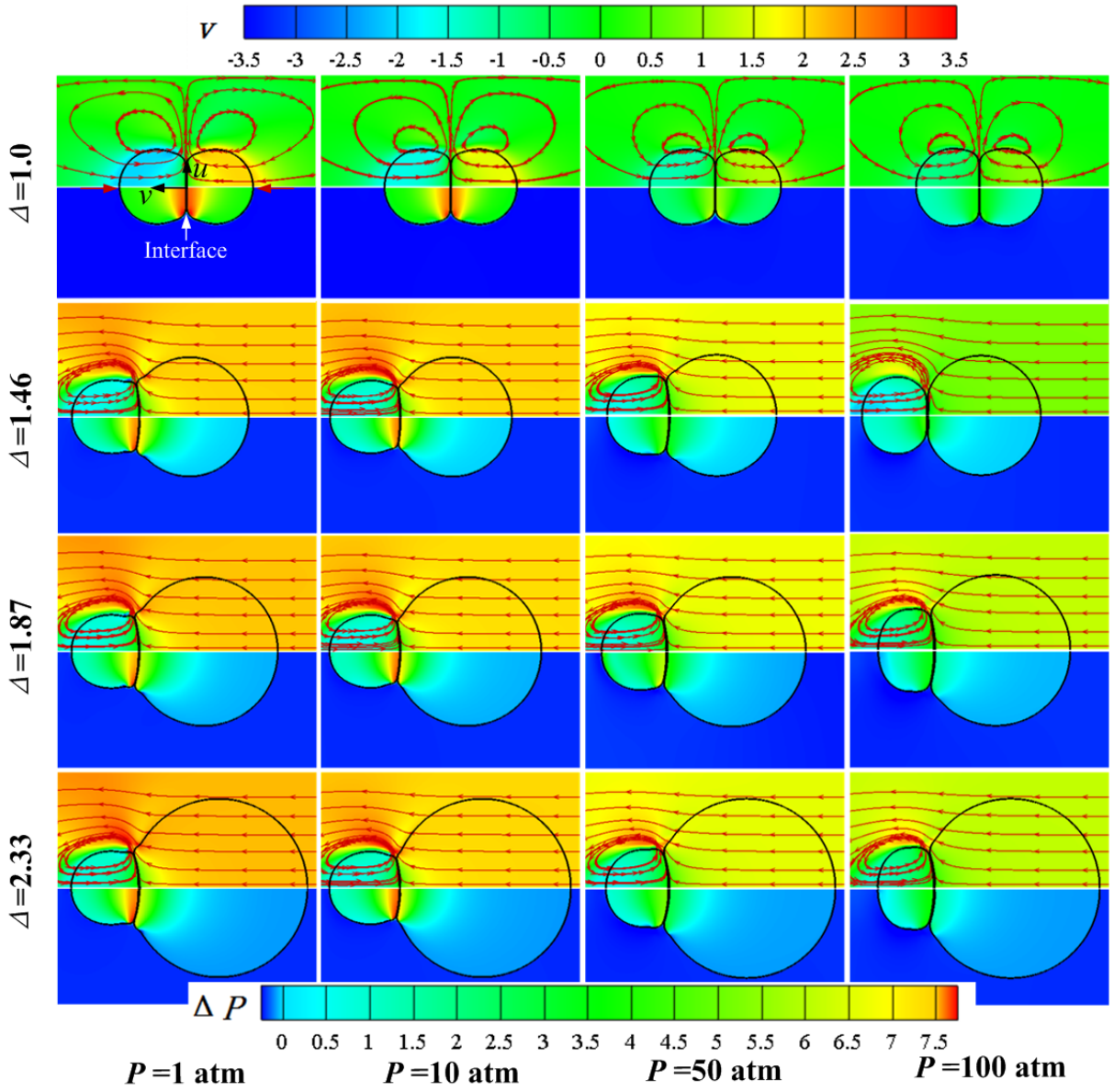

Figure 5. Vertical velocity component, v, (on the top half) and pressure difference between liquid and gas phase, ΔP, (on the bottom half) for various Δ and ambient pressure at maximum TVDR time instant. We=7.3, Oh= 0.775.

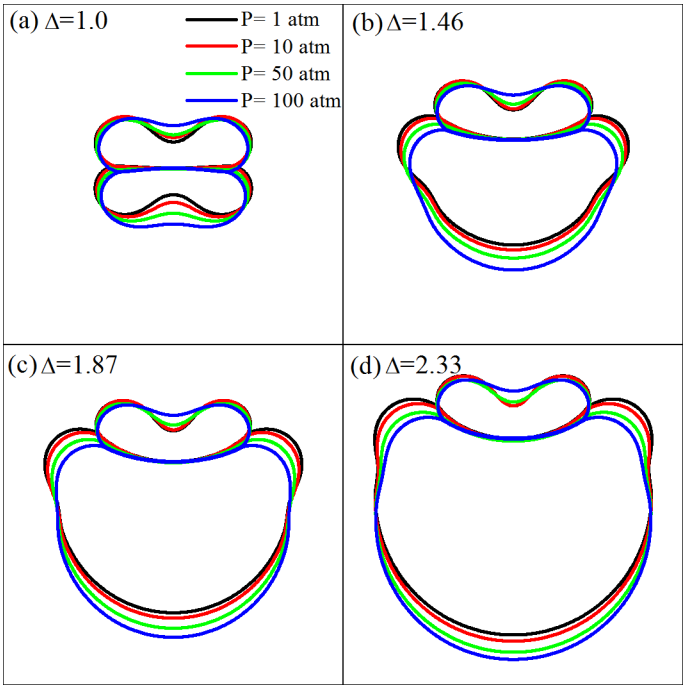

Figure 6. Maximum droplet deformation for n-tetradecane droplets under different ambient pressures. *We*=7.4, *Oh*= 0.775 for (a) Δ=1.0, (b) Δ=1.46, (c) Δ=1.87 and (d) Δ=2.33.

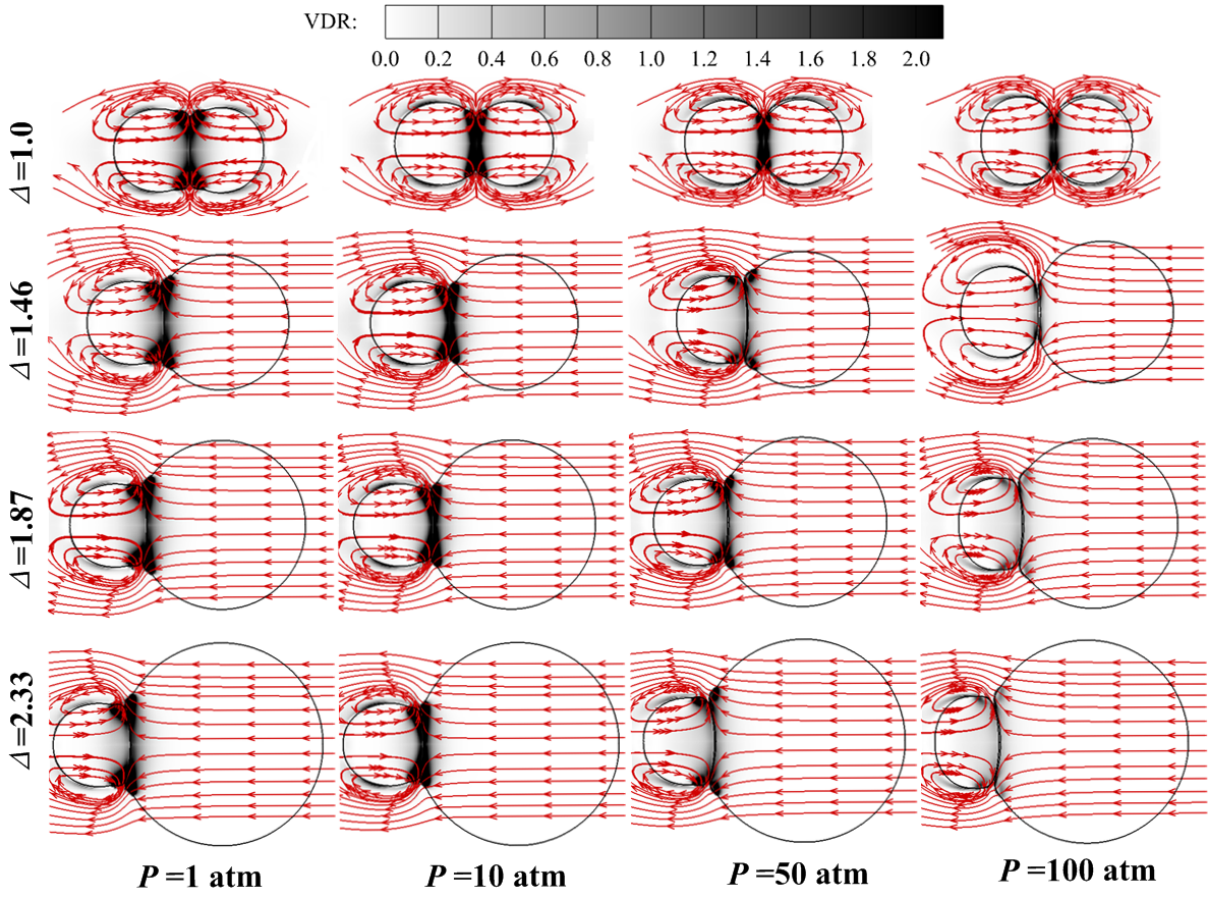

Figure 7. Viscous dissipation rate (VDR) distribution in the colliding droplets for various Δ and ambient pressure at maximum TVDR time instant. We=7.3, Oh= 0.775.

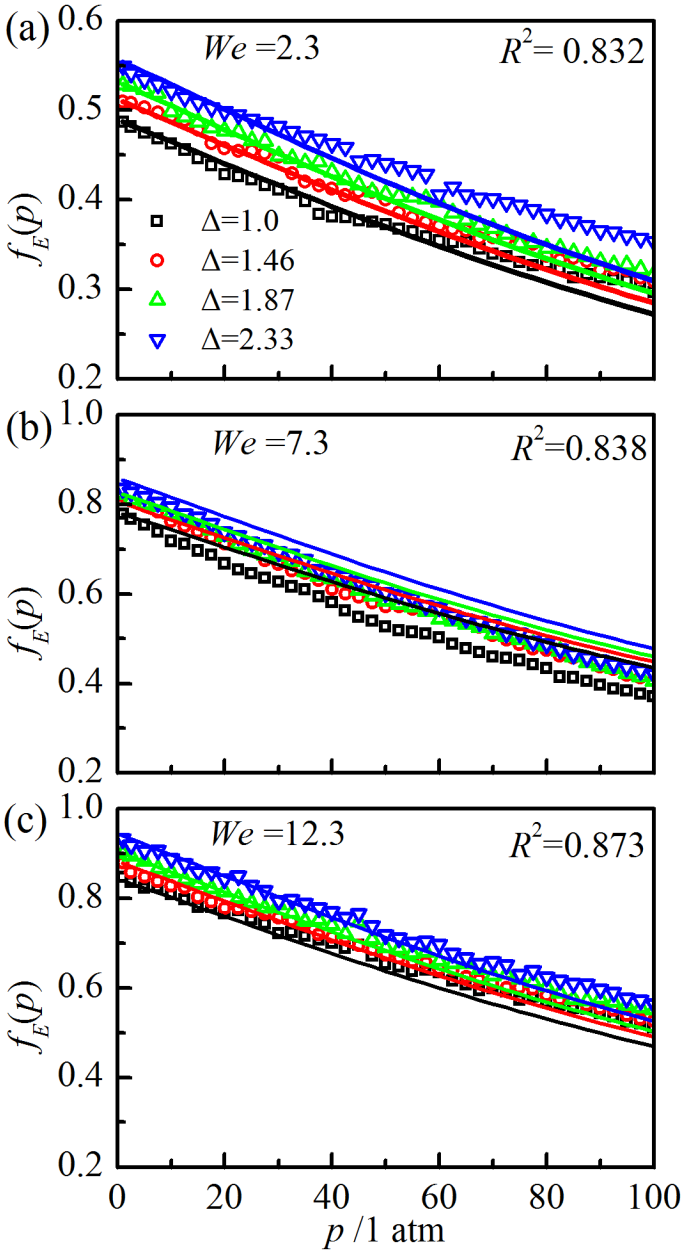

Figure 8. Variation of the energy dissipation fraction, $f_E(p)$, with ambient pressure at the bouncing time. Symbols denote the simulated results and solid lines denote the fitting functions. $f_E(p) = f_E(1)/[a(p-1)^2 + b(p-1) + 1]$, $a = 1.6 \times 10^{-5}$, $b = 5 \times 10^{-3}$. (a) *We* = 2.3 with R^2 =0.832, (b) *We* = 7.3 with R^2 =0.838 and (c) *We* = 12.3 with R^2 =0.873.

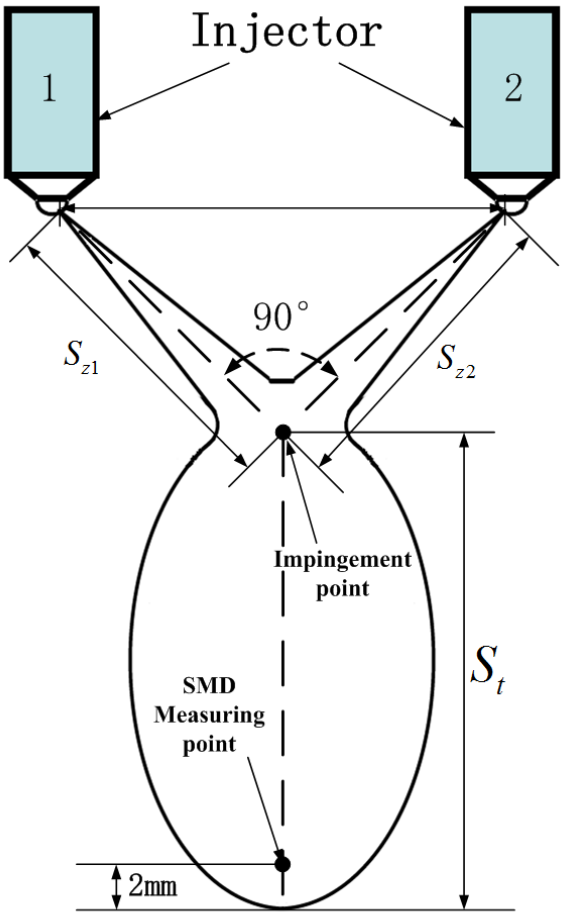

Figure 9. Schematic and SMD measuring point of impinging spray in Chiba et al.'s (2001) experiment at 10 atm.

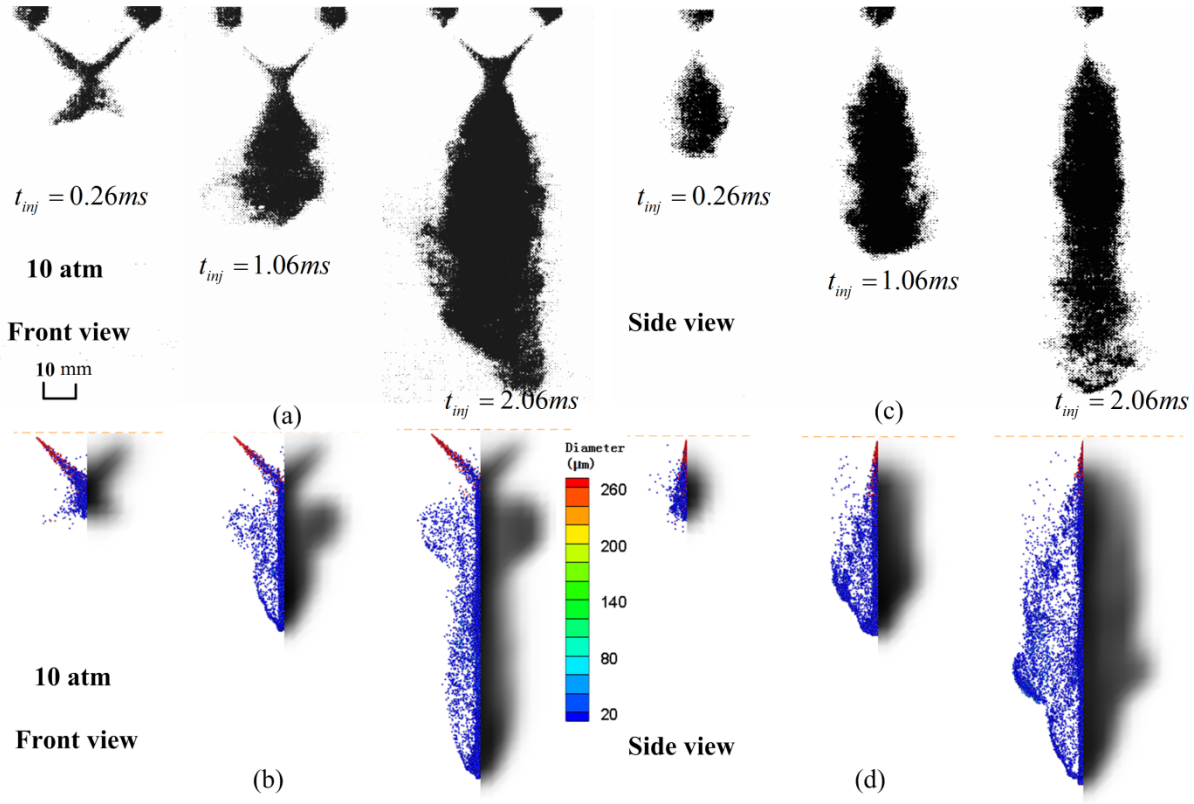

Figure 10. Evaluation of impinging sprays with S_{z1}= S_{z2}=14 mm at 10 atm for (a) and (b) front view and (c) and (d) side view. (a) and (c) experimental shadowgraph images in Maruyama et al.'s (2001) experiment; (b) and (d) Lagrangian droplet parcels predicted by present f_E (p). In simulation graphs, the Lagrangian droplet parcels with droplet size contour are shown in the left half and the numerical shadowgraphs shown in the right half.

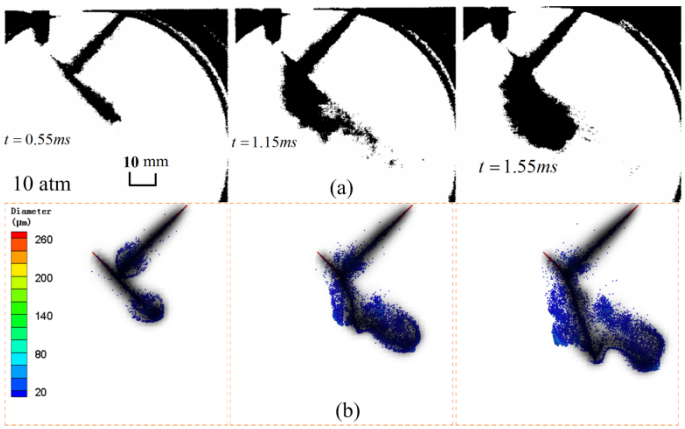

Figure 11. Evaluation of impinging sprays with S_{z1}=15 mm and S_{z2}=45 mm at 10 atm. (a) experimental shadow images in Maruyama et al.'s (2001) experiment; (b) the numerical predictions from f_E (p).

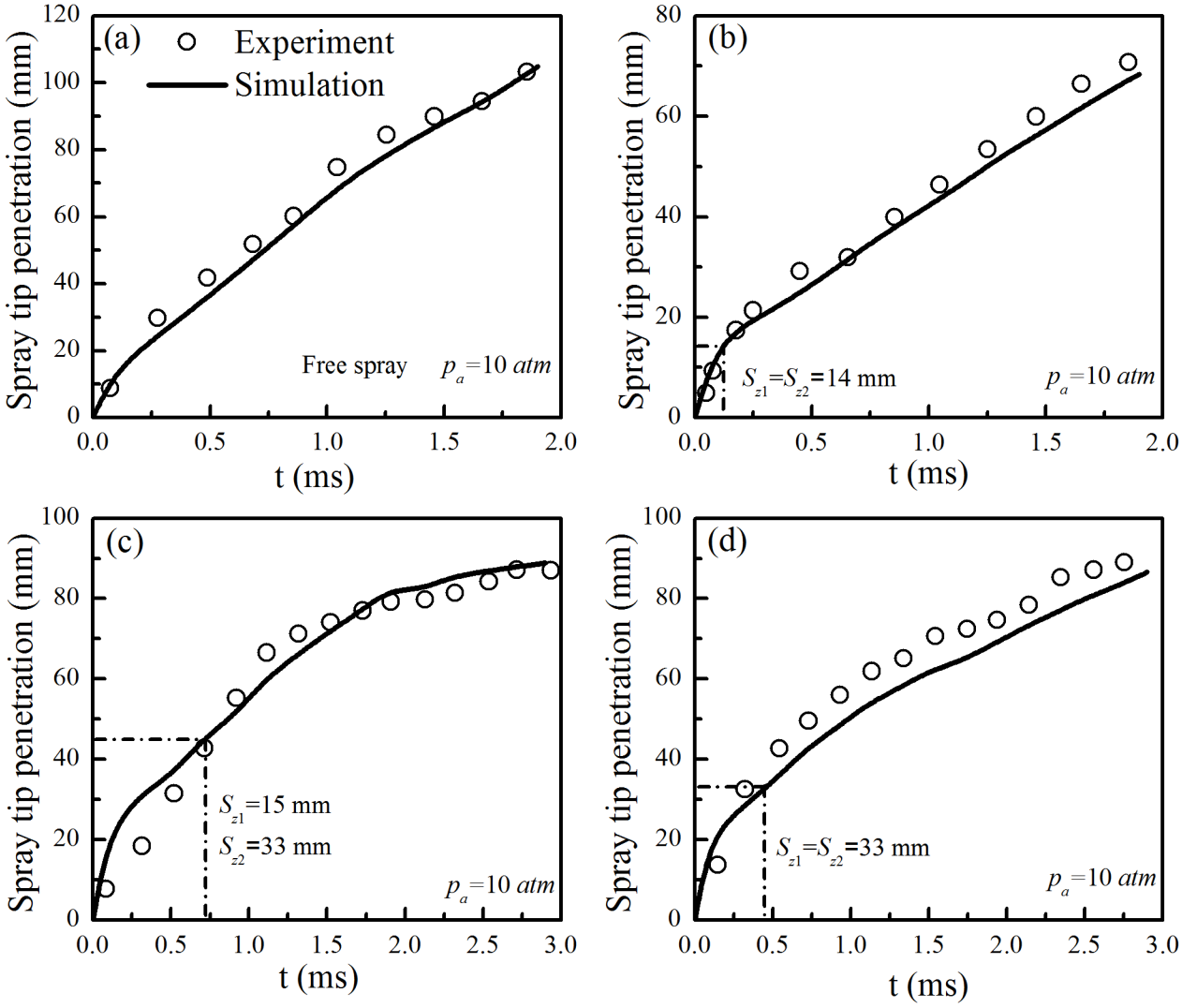

Figure 12. Spray tip penetration length of impinging sprays at 10 atm nitrogen for (a) free spray and impinging sprays of (b) S_{z1}= S_{z2}=14 mm, (c) S_{z1}=15 mm and S_{z2}=45 mm, and (d) S_{z1}= S_{z2}=33 mm. The impingement point and time are also indicated in the graphs.

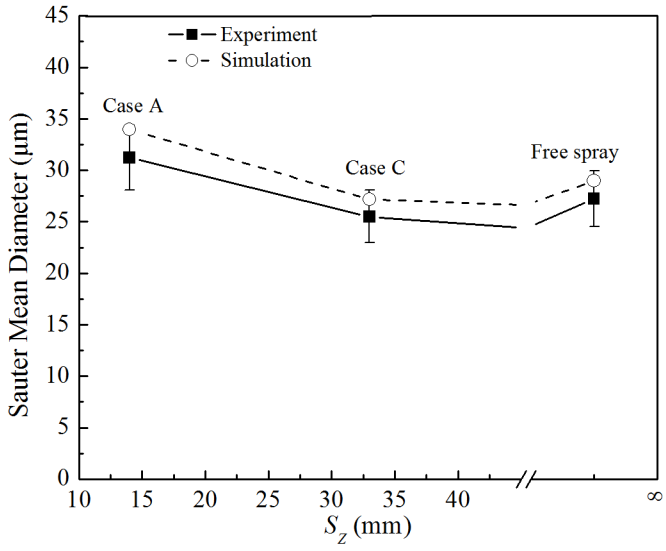

Figure 13. Sauter mean diameter (SMD) at measuring point (i.e., 2 mm above the spray tip) at t =2.0 ms for free spray and impinging sprays of Maruyama et al. (2001).